Journal of
Synchrotron
Radiation

ISSN 0909-0495

Received 9 April 2006
Accepted 9 August 2006

X-ray optics for liquid surface/interface spectrometers

V. Honkimäki,[a] H. Reichert,[b]* J. S. Okasinski[b] and H. Dosch[b]

[a]European Synchrotron Radiation Facility, F-38043 Grenoble, France, and [b]Max-Planck-Institut für Metallforschung, Heisenbergstr. 3, D-70569 Stuttgart, Germany. E-mail: reichert@mf.mpg.de

A new X-ray optics which enables precise structural investigations of liquid surfaces/interfaces is introduced. The new device is based on the use of high-energy microbeams and gives access to large momentum transfer values perpendicular to the liquid surface/interface. The performance of a prototype of this new optics, which has been constructed and implemented at the high-energy diffraction beamline ID15A at the European Synchrotron Radiation Source, is demonstrated.

Keywords: X-ray optics; liquid spectrometer; high-energy X-rays.

1. Introduction

X-ray studies of free surfaces and buried interfaces require particularly specialized instrumentation in order to handle the geometrical constraints, as well as the complex sample environment. Since a liquid surface/interface cannot be tilted with respect to a fixed incident beam, it is a particularly demanding case because the direction of the incident beam must be changed with respect to the liquid surface/interface. The main task of a liquid surface/interface X-ray spectrometer is therefore to provide a primary beam which can be tilted with high precision with respect to the liquid surface/interface.

Following the early designs of liquid surface spectrometers at rotating anodes (Weiss *et al.*, 1986) and at synchrotron radiation sources (Pershan & Als-Nielsen, 1984; Als-Nielsen, 1999; Pershan *et al.*, 1987), a number of dedicated angle-dispersive liquid surface and interface spectrometers have been commissioned in the last few years at several second- and third-generation facilities (Smilgies *et al.*, 2005; Schlossman, 1997; Lin *et al.*, 2003; Ocko *et al.*, 1997). In these designs an additional single crystal is used to tilt the primary X-ray beam with respect to the liquid surface/interface. Since the incident beam moves vertically and horizontally when the incidence angle to the surface is varied, both the sample and detector positions have to follow the moving incident X-ray beam for each angle setting. This usually causes stability problems as liquid surfaces/interfaces are sensitive to mechanical disturbances. For example, it may take a fraction of a minute for the surface waves to be damped out after moving the sample.

Here we demonstrate a new X-ray optical device which turns a conventional diffractometer into a liquid surface/interface spectrometer. By using a matching pair of deflecting crystals, the incident X-ray beam remains centered at a stationary sample position while the incident angle with respect to the surface is varied. This allows one to perform liquid surface/interface scattering experiments using conventional diffractometers without moving the samples during the experiments. The new optics has been implemented at the high-energy diffraction beamline ID15A at the European Synchrotron Radiation Facility (ESRF, Grenoble, France).

Furthermore, our new device is operated with high-energy X-ray beams which are the ideal probe for deeply buried liquid–liquid interfaces. Note that many of the studies of molecular ordering at liquid–liquid interfaces have been performed on Langmuir monolayers (Als-Nielsen *et al.*, 1994), owing partly to the difficulties in probing deeply buried interfaces at conventional X-ray energies. Only recently, buried liquid–liquid interfaces have been studied in more detail (Tikhonov *et al.*, 2004; Schlossman, 2005).

2. Principle and design parameters

Most experimental end-stations at today's synchrotron radiation sources employ double-crystal monochromators with a pair of silicon crystals in (111) orientation. Such a device does not deflect the incident X-ray beam with respect to a sample surface. In order to vary the direction of the incident beam, we have added additional optical components to the standard geometry of double-crystal monochromators. The optics design was guided by six requirements. It should (i) allow the X-ray beam to be tilted such that (ii) the beam stays centered on a stationary sample. The beam size should (iii) be largely unaffected by the optics while (iv) keeping the incident flux at a maximum. In addition, the optical device should (v) be compact for easy incorporation into a standard diffraction set-up and (vi) the background should be kept at a minimum.

The principle of the optical device for the variation of the vertical angle with respect to the surface/interface without changing the sample position is shown in Fig. 1. A first monochromator crystal (C_1) is used to deflect the incident beam. Subsequently, the beam is reflected by a second crystal (C_2) using, however, a higher-order reflection such that the

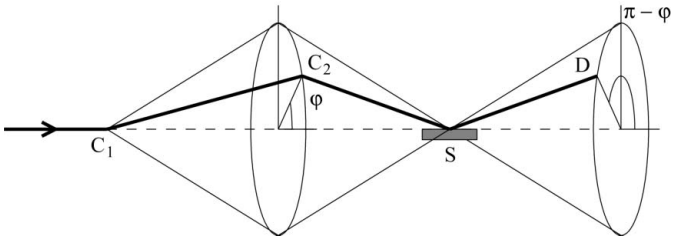

Figure 1
The incident radiation (thick line) is reflected by the first crystal C_1 and subsequently with a larger Bragg angle by the second crystal C_2. By rotating the two crystals in a coupled motion around the incident beam (dashed line), the vertical angle of the incident beam on the sample (S) changes. The detector (D) follows the reflected beam from the sample at the polar angle $\pi - \varphi$ upon rotating both crystals by the angle φ.

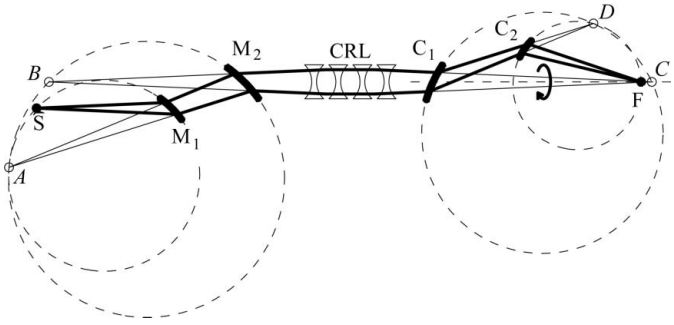

Figure 2
The thick lines show the path of the X-ray beam. Thin lines trace the paths to the focal points (*A*, *B*, *C* and *D*), which are listed in Table 1. The Rowland circles of the bent crystals are shown as dashed lines. By rotating the last two crystals around the axis along the incident beam, the vertical angle of the incident beam to the sample can be manipulated.

double-reflected beam crosses the incident beam at the sample position. The vertical angle α with respect to the sample surface and the angle φ between the reflection plane and the horizontal plane is then determined by

$$\sin\alpha = \sin\varphi \sin 2\Delta\theta, \tag{1}$$

where $\Delta\theta$ is the difference between the Bragg angles of the two crystals C_1 and C_2. Varying φ from 0 to 90° tunes the incidence angle from 0 to a maximum value of $\alpha = 2\Delta\theta$. The maximum momentum transfer q_z perpendicular to the surface is therefore determined by $2\Delta\theta$.

In order to change the incident angle α on the surface/interface, the two crystals C_1 and C_2 must then be rotated in a coupled motion by the angle φ. Since the incident beam moves on a cone with the sample position as the only stationary point, the detector position defining a zero scattering angle must be reset at each incident angle setting. This device satisfies the requirements (i) and (ii) defined above.

In this scheme the beam properties, such as energy bandwidth, size and divergence, are strongly coupled with the maximum reflectivity of the crystals. For an independent optimization of all these parameters, we have separated the monochromatization of the primary beam, the focusing of the beam, and the crystal optics tilting the beam into three independent optics devices. The set-up of all optical components is shown in Fig. 2. It is most stable for small deflection angles, *i.e.* for high photon energies. In order to satisfy the requirements (v) and (vi), we use an additional set of horizontally reflecting pre-monochromators (M_1, M_2) located in the optics hutch and position the two crystals C_1 and C_2 close to the sample in the experimental hutch. The white synchrotron beam is then confined to the optics hutch to minimize the background in the experimental hutch.

The beam size has to be kept as small as possible in order to minimize the footprint of the beam on the surface/interface. For this purpose we use a compound refractive lens (CRL) as a separate optical component to focus the incident beam at the sample position. In order to tune the bandwidth and the incident flux, all crystals (M_1, M_2, C_1, C_2) are asymmetrically cut and bent Laue crystals. The pre-monochromators are arranged in a non-dispersive geometry, *i.e.* the reflections and the asymmetric cuts of the pre-monochromator crystals are equal. This set-up provides an optimized beam for subsequent focusing by the CRL. For a compact and robust design, the second set of crystals (C_1 and C_2) is positioned close to the sample ($\sim$1 m) satisfying requirement (v).

In the following we derive the conditions for optimizing the energy band and the reflectivity of the crystals [requirements (iii) and (iv)]. The relative energy-band due to the bending of the crystal is given by (Schulze & Chapman, 1995; Suortti *et al.*, 2001)

$$\frac{\Delta E}{E} = \frac{T\tan\chi}{\rho\sin 2\theta}\left[2 + (\cos 2\theta + \cos 2\chi)\left(1 - \frac{s_{23} + s_{34}\cot\chi}{s_{33}}\right)\right], \tag{2}$$

where s_{23}, s_{33} and s_{34} are the elastic compliances (dependent on the orientation of the crystal), χ is the angle between the reflecting planes and the crystal surface (asymmetry cut), ρ is the bending radius and T is the crystal thickness. For strongly bent crystals the reflectivity decreases significantly. Neglecting absorption in the crystal, the reflectivity is given by

$$R \propto 1 - \exp(-|\rho/\rho_c|), \tag{3}$$

where the critical bending radius ρ_c is determined by (Authier & Balibar, 1970)

$$\rho_c = \frac{V_{uc}^2}{r_e^2\lambda^3 F_{hkl}^2}\frac{\sin\chi\tan\theta\,(\cos 2\theta + \cos 2\chi)^{1/2}}{2^{1/2}} \times \left[2 + (\cos 2\theta + \cos 2\chi)\left(1 - \frac{s_{23} + s_{34}\cot\chi}{s_{33}}\right)\right]. \tag{4}$$

r_e denotes the classical electron radius, V_{uc} the volume of the unit cell, λ the X-ray wavelength and F_{hkl} the structure factor of the reflection (*hkl*). When the crystal is bent to the critical bending radius in order to keep the equatorial focus as close as possible to the sample position without losing reflectivity, the energy band [see (2)] is given by

$$\frac{\Delta E}{E} = r_e^2\frac{T\lambda^3 F_{hkl}^2}{2^{1/2}\,V_{uc}^2\cos\chi\sin^2\theta\,(\cos 2\theta + \cos 2\chi)^{1/2}}. \tag{5}$$

For small Bragg angles, *i.e.* high photon energies, this simplifies to

Table 1
Focal points, reflections, Bragg angles, asymmetry cuts, focal-point distances, bending radii, critical bending radii, crystal thicknesses, maximum reflectivities and the bandwidth for the optical elements.

The real and virtual focal points are indicated by subscripts R and V, respectively.

	M_1	M_2	CRL	C_1	C_2	C_1'	C_2'
Source	S_R	A_R	B_R	C_V	D_V		
Focus	A_V	B_V	C_R	D_R	F_R		
hkl	111	111		111	220	111	220
θ (°)	1.596	1.596		1.596	2.606	1.596	2.606
χ (°)	37.7	−37.8		−10.0	10.0	−10	30
p (m)	56.0	59.4	62.00	1.30	0.67	3.58	8.37
q (m)	58.5	56.9	4.00	1.31	0.66	3.62	8.10
ρ (m)	69.3	76.8		1.31	0.69	3.62	9.93
ρ_c (m)	8.2	7.7		3.6	4.5	3.62	9.93
T (mm)	5.0	5.0		1.0	0.5	1.0	1.5
R_{max}	0.76	0.69		0.28	0.13	0.59	0.56
ΔE (eV)	256	217		765	451	278	266

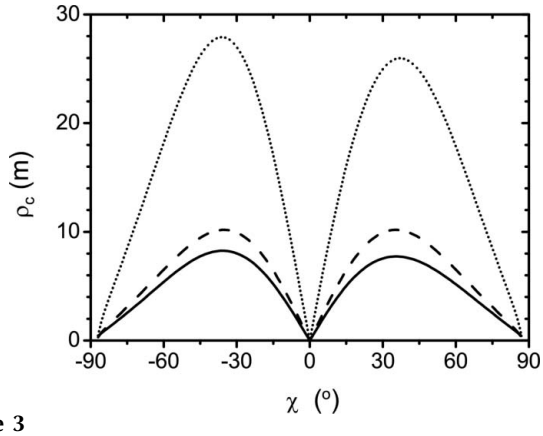

Figure 3
Critical bending radius at 71 keV for the (111) reflection (solid line), the (220) reflection (dashed line) and the (311) reflection (dotted line) of silicon as a function of the asymmetric cut χ.

$$\frac{\Delta E}{T} \simeq 2r_e^2 \frac{hcF_{hkl}^2 d_{hkl}^2}{V_{uc}^2 \cos^2\chi} = \frac{c_{hkl}}{\cos^2\chi}, \qquad (6)$$

where h denotes Planck's constant, c the speed of light and d_{hkl} the lattice spacing for the reflection (*hkl*). Note that the result is independent of the incident energy. The constants c_{hkl} in (6) for the first three reflections of silicon are $c_{111} = 262$ eV mm^{-1}, $c_{220} = 129$ eV mm^{-1} and $c_{311} = 40$ eV mm^{-1}. Fig. 3 shows the critical bending radius at an energy of 71 keV for the (111), the (220) and the (311) reflection of silicon as a function of the asymmetry cut χ. A typical set of parameters for the optics set-up is summarized in Table 1 for an X-ray energy of 71 keV.

For optimum focusing conditions, the bending radii of the crystals C_1 and C_2 are small, 1.3 m and 0.7 m, respectively, implying a poor maximum reflectivity. A small bending radius also affects the reflected energy-band. Rather than optimizing the equatorial focusing conditions we arrange the set-up such that the incident flux will be optimized. We have calculated the reflectivities for all monochromator crystals. For the reflectivities depicted in Fig. 4(*a*) the parameters were chosen such that the equatorial focus of the crystals is kept at the sample position to minimize the beam size at the sample position. In

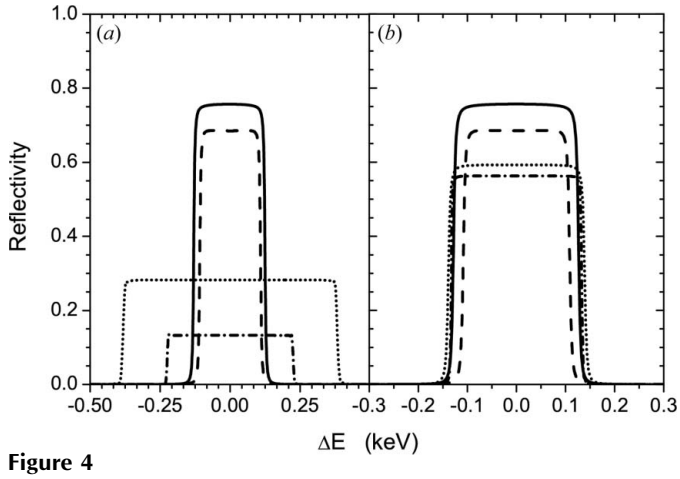

Figure 4
Calculated reflectivities of the pre-monochromator crystals M_1 (solid lines) and M_2 (dashed lines) and the monochromator crystals C_1 (dotted lines) and C_2 (dashed-dotted lines) with (*a*) the equatorial focus optimized and (*b*) the total reflected intensity optimized.

Fig. 4(*b*) we show the calculated reflectivities (Schulze & Chapman, 1995) for all the monochromator crystals with the parameters optimized for maximum reflectivity (see Table 1). The columns headed C_1 and C_2 in Table 1 list the parameters for optimized focusing, while the columns headed by C_1' and C_2' are optimized for intensity.

3. Instrumentation

We have implemented the optics device at the high-energy beamline ID15A at the ESRF. The X-ray source is an asymmetric permanent-magnet wiggler with a critical energy of 44 keV. The distance between the source and the first pre-monochromator crystal in the optics hutch is 56 m. The distance between the two pre-monochromator crystals is given by $d = \Delta y \cot 2\theta$, with the equatorial off-set of the beam chosen as $\Delta y = 50$ mm. Details about the pre-monochromators and the focusing CRL (commercially available from RWTH Aachen) can be found elsewhere (Suortti *et al.*, 2001; Reichert *et al.*, 2003).

The optics station for the crystals C_1 and C_2 is independent of the other beamline components and can be easily included in the set-up. The optics set-up carrying crystals C_1 and C_2 is depicted in Fig. 5. All crystals have been supplied by the optics group of the ESRF. Both crystals C_1 and C_2 are mounted on separate rotation stages and bent by linear translations that push against the tip of the triangular Si crystals. We have chosen a triangular shape for crystals C_1 and C_2 in order to achieve isoclastic bending. Both rotation stages are mounted on a rail such that the incident beam on crystal C_1 is aligned with the rotation axis of the Eulerian cradle defining the polar angle φ. This assembly is mounted on a rotation stage on top of a table with two vertical linear drives. This geometry allows one to center the rotation axis φ of the Eulerian cradle along the incident beam.

The incoming beam is monitored at two separate positions, after the CRL and directly after crystal C_2. All beams which

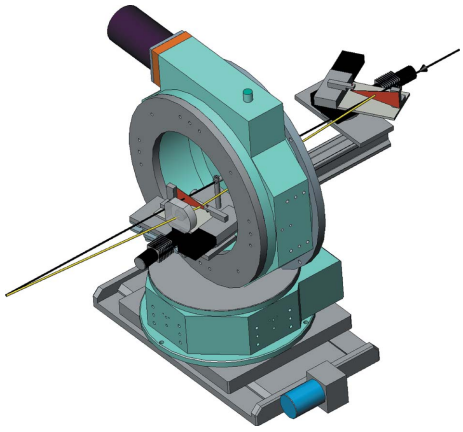

Figure 5
Representation of the tilt monochromator assembly. As may be seen, the black line denotes the undeflected beam on the rotation axis of the Eulerian cradle, while the yellow line marks the path of the beam deflected by the two triangular crystals C_1 and C_2 at an incident angle $\alpha = 0$.

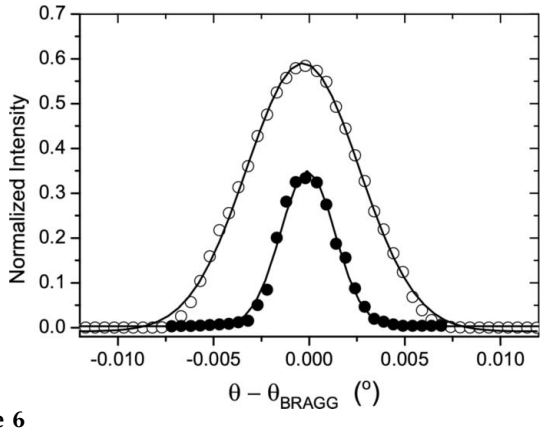

Figure 6
Normalized rocking curve of crystal C_1 (open circles) and of crystal C_2 after the beam passed through crystal C_1 (filled circles).

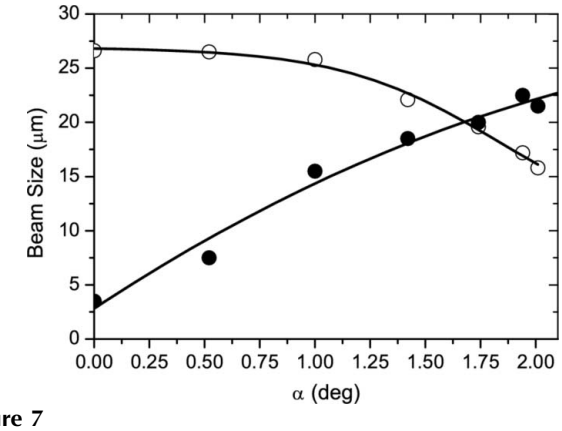

Figure 7
Variation of the horizontal beam size (open circles) and the vertical beam size (filled circles) at the sample position. The lines are polynomial fits to the data.

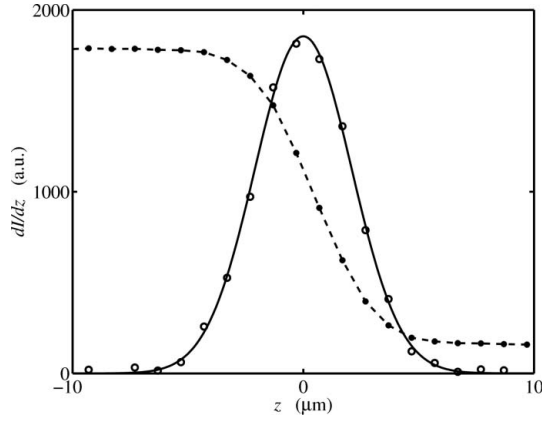

Figure 8
Knife-edge scan of the incident beam in the vertical direction (filled circles) at the sample position. The derivative of the knife-edge scan defines the beam shape in the vertical direction (open circles). The solid line is a Gaussian fit to the beam shape with a FWHM of 5 μm.

are transmitted directly through the crystals M_1, M_2, C_1 and C_2 are followed and absorbed by separate beam stops.

4. Performance

In the following we demonstrate the performance of the set-up. For the experimental results shown below, we have used the configuration M_1 = Si(111), M_2 = Si(111), C_1 = Si(111) and C_2 = Si(220) at an X-ray energy of 71 keV. The crystals M_1 and M_2 are 5 mm thick, while the crystals C_1 and C_2 are 0.9 mm thick. For focusing we have used a CRL with 256 individual Al lenses in order to achieve a vertical focus of 4 μm at $\alpha = 0$. Fig. 6 shows the normalized rocking curves of the crystal C_1' and of the crystals C_1' and C_2' combined, where the rocking curves have been normalized to the intensity after the pre-monochromators M_1 and M_2. We achieve a transmission of 33% through the additional crystals C_1' and C_2', which is completely optimized, although the thicknesses of the available crystals C_1' and C_2' were somewhat smaller than the values given in Table 1. This has been compensated in the current set-up by slightly overbending both crystals C_1 and C_2.

At $\alpha = 0$ all four crystals are bent horizontally providing optimum vertical focusing conditions with the horizontal focus located behind the sample. Since the crystals C_1 and C_2 are rotated in a coupled motion to increase the incident angle α, the reflecting planes of C_1 and C_2 change from the horizontal plane to a vertical plane. Therefore, the horizontal and the vertical size of the beam change as the incidence angle α is varied (see Fig. 7). The vertical beam size increases with α, while the horizontal beam size decreases.

The shape of the beam is well defined and remains Gaussian over the whole range of incidence angles α. Fig. 8 shows the vertical beam profile measured in a knife-edge scan at the sample position with $\alpha = \varphi = 0$.

A very important quantity for the design of sample cells and the data analysis is the length of the footprint on the sample surface. Since the equatorial focus is off from the sample position and the optimum focusing conditions are increasingly violated for larger incidence angles α, the variation of the length of the footprint is much smaller for the new set-up using the additional crystals C_1 and C_2 (see Fig. 9). The length of the footprint is, in fact, almost constant after an initial decrease at

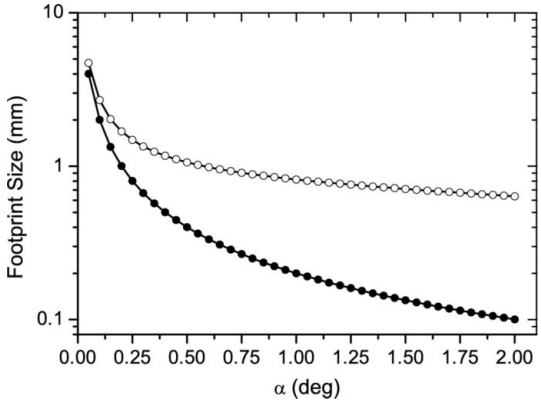

Figure 9
Variation of the length of the footprint on the sample surface/interface as a function of the incidence angle α for the conventional set-up using M_1 and M_2 (filled circles) and with the additional crystals C_1 and C_2 (open circles).

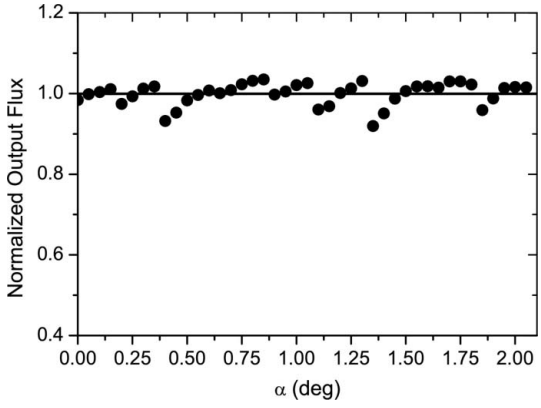

Figure 10
Variation of the incident flux at the sample position as a function of the incidence angle α using the additional crystals C_1 and C_2 for inclining the beam.

small angles α. Measurements of the reflectivity of surfaces/interfaces can, therefore, be performed in a more consistent way, since the incoming X-ray beam is averaging over the same sample area, which is particularly important in the presence of sample surface/interface heterogeneities.

The X-ray flux at the sample position is determined by the accuracy of the alignment of all optical elements in the beam and their mechanical stability. Fig. 10 shows the measured flux at the sample position for an X-ray energy of $E = 71$ keV. The absolute photon flux varies between 2×10^{10} photons s^{-1} and 5×10^{10} photons s^{-1} depending on the focusing conditions. The variation of the incidence flux is $\sigma = 3\%$ over the entire range of incidence angles, which allows one to reach a maximum vertical momentum transfer of 2.53 $Å^{-1}$ with a combination of a Si(111) (C_1) and a Si(220) crystal (C_2). The remaining fluctuations are due to the fine-tuning of the crystal C_2 to compensate for the wobbling of the Eulerian cradle (the jumps correspond to a single motor step). They can be removed by normalizing the scattered X-ray intensity to an incident beam monitor located between the last crystal C_2 and the sample position (see Fig. 5).

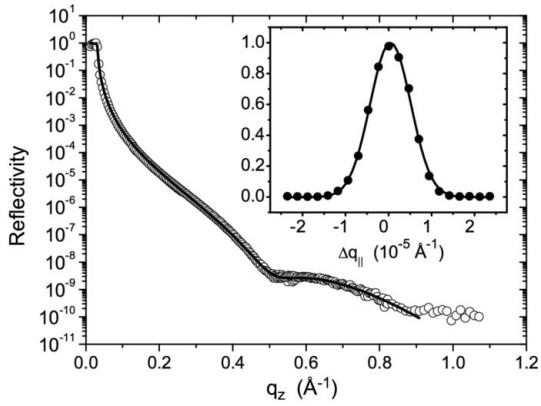

Figure 11
Reflectivity from a fused silica surface (open circles) together with a fit (solid line) using the Parrat formalism. The inset shows the normalized intensity profile of the reflected beam parallel to the surface at a perpendicular momentum transfer $q_z = 0.17$ $Å^{-1}$.

Finally, we demonstrate the performance of the optics set-up by measurement of the reflectivity from a standard fused silica sample (supplied by Wave Precision). The sample was disc-shaped with a diameter of 25 mm and a thickness of 10 mm. The sample was kept in air and remained stationary during the measurements. The momentum transfer q_z perpendicular to the surface was varied by scanning the angle φ with the crystals C_1 and C_2 in a coupled motion while tracking the reflected beam with the detector. Fig. 11 shows the measured reflectivity with a dynamic range of ten orders of magnitude up to a maximum momentum transfer $q_z = 1$ $Å^{-1}$. The profile of the reflected beam parallel to the sample surface at $q_z = 0.17$ $Å^{-1}$ is shown in the inset. The width of the in-plane scan of 1×10^{-5} $Å^{-1}$ demonstrates the very high quality of the sample surface and the superior resolution of the instrument. Fitting the reflectivity with the standard Parratt formalism (Parratt, 1954) confirms the presence of a thin water/organic film (thickness 6.1 Å, roughness 3.1 Å) on top of the strongly hydrophilic silica surface (roughness 2.9 Å).

5. Conclusion

We have demonstrated that the new tilt stage provides a very clean and stable beam for structural investigations of liquid surfaces and interfaces. The use of a high-energy X-ray source allows one to study deeply buried interfaces as well as free surfaces. The set-up is very compact and can be easily added to existing optical set-ups. Furthermore, the optics device is ideally suited for experiments where the sample has to be kept stationary during the measurements. This may be the case in experiments where structural investigations with an X-ray beam are combined with other experimental techniques which require a stationary sample environment, *e.g.* a real-space scanning probe experiment combined with reciprocal-space diffraction measurements. We have tested the new optical scheme at high X-ray energies. By using thin silicon crystals it should be possible to extend the energy range to lower X-ray energies, allowing one to cover the absorption edges of many elements.

We would like to thank Mogens Kretzschmer (ESRF) for his support in the design and the construction of the new optics set-up. We also thank the Max Planck Society for funding the construction of the instrumentation.

References

Als-Nielsen, J. (1999). *Synchrotron Rad. News*, **12**, 5.
Als-Nielsen, J., Jacquemain, D., Kjaer, K., Leveiller, F., Lahav, M. & Leiserowitz, L. (1994). *Phys. Rep.* **246**, 252–313.
Authier, A. & Balibar, F. (1970). *Acta Cryst.* A**26**, 647–654.
Lin, B., Meron, M., Gebhardt, J., Graber, T., Schlossman, M. L. & Viccaro, P. J. (2003). *Physica B*, **336**, 75–80.
Ocko, B. M., Sirota, E. B., Sinha, S. K., Gang, O. & Deutsch, M. (1997). *Phys. Rev. E*, **55**, 3164–3182.
Parratt, L. G. (1954). *Phys. Rev. B*, **95**, 359–369.
Pershan, P. S. & Als-Nielsen, J. (1984). *Phys. Rev. Lett.* **52**, 759–762.
Pershan, P. S., Braslau, A., Weiss, A. H. & Als-Nielsen, J. (1987). *Phys. Rev. A*, **35**, 4800–4813.
Reichert, H., Honkimäki, V., Snigirev, A., Engemann, S. & Dosch, H. (2003). *Physica B*, **336**, 46–55.
Schlossman, M. L. (1997). *Rev. Sci. Instrum.* **68**, 4372–4384.
Schlossman, M. L. (2005). *Physica B*, **357**, 98–105.
Schulze, C. & Chapman, D. (1995). *Rev. Sci. Instrum.* **66**, 2220–2223.
Smilgies, D. M., Boudet, N., Struth, B. & Konovalov, O. (2005). *J. Synchrotron Rad.* **12**, 329–339.
Suortti, P., Buslaps, T., Honkimäki, V., Kretzschmer, M., Renier, M. & Shukla, A. (2001). *Z. Phys. Chem.* **215**, 1419–1435.
Tikhonov, A. M., Pingali, S. V. & Schlossman, M. L. (2004). *J. Chem Phys.* **120**, 11822–11838.
Weiss, A. H., Deutsch, M., Braslau, A., Ocko, B. M. & Pershan, P. S. (1986). *Rev. Sci. Instrum.* **57**, 2554–2559.